HHS Public Access

Author manuscript

IEEE Access. Author manuscript; available in PMC 2024 December 05.

Published in final edited form as:

IEEE Access. 2024 ; 12: 135730–135745. doi:10.1109/access.2024.3449811.

MRI Denoising Using Pixel-Wise Threshold Selection

NIMESH SRIVASTAVA[1,2], **GYANA RANJAN SAHOO**[1], **HENNING U. VOSS**[3], **SUMIT N. NIOGI**[3,4], **JACK H. FREED**[1,5], **MADHUR SRIVASTAVA**[1,5,6] **[Member, IEEE]**

[1]Department of Chemistry and Chemical Biology, Cornell University, Ithaca, NY 14853, USA

[2]EZ Diagnostics Inc., Ithaca, NY 14850, USA

[3]Cornell MRI Facility, College of Human Ecology, Cornell University, Ithaca, NY 14853, USA

[4]Department of Radiology, Weil Cornell Medicine, New York-Presbyterian Hospital, New York City, NY 10065, USA

[5]National Biomedical Center for Advanced Electron Spin Resonance Technology, Cornell University, Ithaca, NY 14853, USA

[6]Cornell Atkinson Center for Sustainability, Cornell University, Ithaca, NY 14853, USA

Abstract

Magnetic resonance imaging (MRI) has emerged as a promising technique for non-invasive medical imaging. The primary challenge in MRI is the trade-off between image visual quality and acquisition time. Current MRI image denoising algorithms employ global thresholding to denoise the whole image, which leads to inadequate denoising or image distortion. This study introduces a novel pixel-wise (localized) thresholding approach of singular vectors, obtained from singular value decomposition, to denoise magnetic resonance (MR) images. The pixel-wise thresholding of singular vectors is performed using separate singular values as thresholds at each pixel, which is advantageous given the spatial noise variation throughout the image. The method presented is validated on MR images of a standard phantom approved by the magnetic resonance accreditation program (MRAP). The denoised images display superior visual quality and recover minute structural information otherwise suppressed in the noisy image. The increase in peak-signal-to-noise-ratio (PSNR) and contrast-to-noise-ratio (CNR) values of ≥ 18% and ≥ 200% of the denoised images, respectively, imply efficient noise removal and visual quality enhancement. The structural similarity index (SSIM) of ≥ 0.95 for denoised images indicates that the crucial structural information is recovered through the presented method. A comparison with the standard filtering methods widely used for MRI denoising establishes the superior performance of the presented method. The presented pixel-wise denoising technique reduces the scan time by 2–3 times and has the potential to be integrated into any MRI system to obtain faster and better quality images.

Corresponding authors: Madhur Srivastava (ms2736@cornell.edu), Jack H. Freed (jhf3@cornell.edu), and Sumit N. Niogi (sun2003@med.cornell.edu).

INDEX TERMS

Magnetic resonance imaging; denoising; image denoising; singular value decomposition; SF-SVD; pixel-wise noise threshold selection; pixel-wise thresholding; peak-signal-to-noise ratio; contrast-to-noise ratio; structural similarity index

I. INTRODUCTION

Magnetic resonance imaging (MRI) is a widely used non-invasive imaging technique that provides detailed structural information and functional characteristics of internal organs. The ability of magnetic resonance imaging to characterize and discriminate tissues using their physical and biochemical properties offers special advantages in clinical diagnosis. Additionally, the technique produces sectional images of similar resolution in any projection plane without moving the patient. Generally, the magnitude of the reconstructed MRI image is used for visual inspection which plays a crucial role in accurate clinical diagnosis. However, the visual quality of the MR image is degraded by the existing noise during the acquisition process [1]. During data collection, the MR images get corrupted by various kinds of noise arising from electronic noise, random signal fluctuation, or faulty detector elements [2]. Depending on the single or multi-channel data collection, noise in MRI is described by white Gaussian noise [3], Rician noise [4], and non-central Chi distribution [5], [6].

Generally, noise reduces the visual quality of the image and masks subtle information, which is problematic, especially in diagnostic imaging. Further, image postprocessing techniques such as image segmentation [7], [8], [9], [10], [11] and predictive analysis [11], [12] are employed for diagnostic feature extraction and classification purposes. However, noise in the image affects the image segmentation and may alter the classification results. In diagnostic imaging, a small variation in image processing might lead to incorrect diagnosis. Hence, efficient denoising of MR images is essential for further processing and accurate diagnosis.

Current denoising techniques employ global thresholding criteria. In global thresholding, the spatial distribution of noise magnitude throughout the image is assumed to be consistent across the image. However, the noise distribution in the MR images follows Gaussian, Rician, or non-central Chi distributions that vary locally and can possess distinct magnitudes between neighboring pixels, which might lead to loss of critical information or distort the pixels with less noise. Hence, a localized denoising approach that treats the noise in individual pixels separately is necessary for efficient denoising of the MR images. The flowchart in Figure 1 illustrates the difference between the global and presented local thresholding approaches.

Here, we present a singular value decomposition (SVD) based MR image denoising method that implements pixel-wise thresholding of singular vectors. It is based on the new approach of Srivastava-Freed singular value decomposition (SF-SVD) that has enabled point-wise processing of two-dimensional data [13], [14]. In this paper, we develop a new localized denoising method to remove noise at each pixel individually by performing pixel-wise thresholding, given that the spatial noise varies throughout the image. The presented pixel-

wise denoising method is applied to the MR images of a commercially available MRAP approved phantom. The denoised images are very similar to the reference images both qualitatively and quantitatively. The algorithm is fast and has the potential to be integrated into any MRI system to reduce acquisition time.

The paper is organized as follows. Section II discusses the previous MRI image denoising algorithms and their limitations in removing noise effectively. In section III, we provide details of the SVD and pixel-wise thresholding of singular vectors to perform denoising. In section IV, we present the parameters used to evaluate denoising results. In section V, we provide details about the ACR phantom and magnetic resonance imaging system used for imaging. Section VI discusses the results and section VII summarizes the findings in the conclusion.

II. RELATED WORKS

In general, denoising of the MR images can be performed in two ways. In the first approach, one averages multiple recorded images of the same sample. However, the collection of multiple images takes a longer time and can introduce motion artifacts. In the second approach, the MR images can be denoised by utilizing a suitable denoising technique that provides a reliable and quick result. To date, numerous MR image denoising algorithms have been presented including the classical spatial and temporal filters [15], anisotropic diffusion filter [16], [17], [18], [19], [20], [21], [22], bilateral and trilateral approaches [23], [24], [25], [26], [27], [28], wavelet transform [29], [30], [31], [32], [33], [34], [35], the curvelet and the contourlet transforms [36], [37], [38], maximum likelihood approach [39], [40], [41], [42], linear minimum mean square error estimation [43], [44], [45], nonparametric neighborhood statistics/estimation [46], [47], [48] and singularity function analysis [49], [50].

Non-local means (NLM) filtering is one of the most widely used MR image denoising techniques [51], [52], [53], [54], [55], [56], [57], [58], [59]. It exploits the redundancy in the image and reduces noise by averaging non-local patches. Also, a modified NLM was utilized to eliminate Rician noise [60]. Furthermore, a two-stage non-local principal component analysis based thresholding method was proposed to denoise the MR images [61]. This method performs a non-local PCA thresholding and then applies a rotationally invariant NLM filter for denoising. Block matching and 3D filtering (BM3D) is a natural extension of the NLM method that utilizes self spatial similarities in the images for denoising [62]. Though the existing methods produce reasonable results in the MR image denoising, they have several limitations such as time consuming operations, loss of critical information, and manual intervention. On the other hand, machine learning techniques can overcome such limitations by quickly and autonomously denoising medical images. Recently, deep learning based approaches have been used to denoise the MR images [63], [64]. However, deep learning methods require a large amount of data for model training and often produce a biased result.

III. PIXEL-WISE THRESHOLDING (PWT)

1) SINGULAR VALUE DECOMPOSITION

Singular value decomposition of a rectangular matrix X_{ij} of dimension $M \times N$ $(i = 1, 2, \cdots, M;\ j = 1, 2, \cdots, N)$ is given by

$$X = U \Sigma V^T \tag{1}$$

where U and V are $(M \times M)$ and $(N \times N)$ unitary matrices of left singular and right singular vectors respectively and $\Sigma = diag(\delta_1, \delta_2, \cdots, \delta_r)$ with $\delta_1 \geq \delta_2 \geq \cdots \delta_r \geq 0$, where δ_r is the singular value corresponding to r^{th} singular vectors. Basically U and V are the eigenvectors of $\left\{XX^T\right\}$ and $\left\{X^TX\right\}$ respectively.

Also X can be expressed in terms of U, V and δ as

$$X_{ij} = \sum_{k=1}^{min(M,N)} U_{ik}\delta_k V_{jk} \tag{2}$$

2) PIXEL-WISE THRESHOLD SELECTION

Currently, given an input image (X), SVD denoising methods threshold singular vectors U and V by using a single singular value threshold (λ) to denoise the image [65], [66]. Singular vectors beyond the thresholding singular value λ are not considered in the reconstruction of the denoised image. This poses a challenge since it can potentially remove critical information and distort pixels with less noise. However, contrary to the truncated SVD, the SF-SVD approach preserves critical information of individual points of the singular vectors [13], [14]. Localized pixel-wise denoising is achieved in this work by selecting and thresholding each pixel of the singular vectors U and V by different singular values λ_{ij}. Figure 2 depicts the flowchart of the presented pixel-wise denoising algorithm.

Equation 2 can be used to perform SVD of the image, then one can denoise the image X by selecting the λ_{ij} threshold for each pixel to obtain the denoised image X'. Each pixel in X' is given by

$$X'_{ij} = \sum_{k=1}^{\lambda_{ij}} U_{ik}\delta_k V_{jk} \tag{3}$$

To obtain the threshold λ_{ij} at any pixel in X'_{ij}, we define a saturation parameter (S) as shown in equation 4.

$$S = \sum_{k=1}^{l} (U_{ik}\delta_k V_{jk})^2 \tag{4}$$

where l is the number of singular values. The parameter S gradually saturates as the sum of $(U_{ik}\delta_k V_{jk})^2$ increases with an increase in l. S will saturate faster for noisy pixels than that of the pixels without noise. The singular vector number l at which the saturation begins is determined as the threshold value required to denoise the pixel. Plots of S vs l at different pixel numbers for images of different slices are displayed in figure 3. The vertical lines inside the figures show the singular value number used to denoise that pixel. It can be seen from the figure 3 that the saturation for noisy pixels occurs at lower singular values.

IV. EVALUATION METRICS

A. PEAK SIGNAL TO NOISE RATIO (PSNR)

Denoised images are evaluated using the peak-signal-to-noise ratio. The PSNR quantifies the amount of noise removed from the corrupted image and is defined as the ratio between the maximum possible power of a signal and the power of the distorting noise. In general, a higher value of PSNR indicates lesser noise in the signal. The PSNR in decibels (db) can be calculated from equation 5.

$$PSNR = 10log_{10}\frac{P^2}{MSE} \tag{5}$$

where P is the maximum possible value of the image and MSE is the mean square error of the denoised image with respect to a reference image which is given by equation 6.

$$MSE = \frac{1}{MN}\sum_{i=1}^{M}\sum_{j=1}^{N}\left[X'_{ij} - R_{ij}\right]^2 \tag{6}$$

where X'_{ij} and R_{ij} are the pixel at index (i, j) in the denoised image X and reference image R respectively.

B. CONTRAST TO NOISE RATIO (CNR)

The quality of the denoised image is determined by contrast to noise ratio. CNR is defined as the ratio between the contrast of the signal to the background and the spread of the distorting noise. In general, a higher CNR value indicates better differentiation between the target structure and the noise. Mathematically, CNR can be expressed as equation 7.

$$CNR = \frac{\mu_{ROI} - \mu_B}{\sigma_{noise}} \tag{7}$$

where μ_{ROI} and μ_B are the mean values of the region of interest (ROI) and background respectively, and σ_{noise} is the standard deviation of the noise.

C. STRUCTURAL SIMILARITY INDEX MEASURE (SSIM)

Structural similarity index measure (SSIM) is used to determine the perceived quality of an image by measuring the similarity between two images [67]. The SSIM value ranges from 0 to 1. The higher the SSIM value greater the similarity between the images, lower the SSIM value lesser the similarity between images. The mathematical formula is given by equation 8

$$SSIM = \frac{(2\mu_X\mu_Y + c_1)(2\sigma_{XY} + c_2)}{(\mu_X^2 + \mu_Y^2 + c_1)(\sigma_X^2 + \sigma_Y^2 + c_2)} \tag{8}$$

where μ_X and μ_Y are mean values of images X and Y respectively, and σ_X and σ_Y are the standard deviations of image X and Y respectively. σ_{XY} is the correlation between image X and Y. $c_1 = (k_1 L)^2$ and $c_2 = (k_2 L)^2$ are constants to stabilize division in case of weak denominators. L is the dynamic range of the pixel values, $k_1 = 0.01$ and $k_2 = 0.03$.

D. ROOT MEAN SQUARE (RMS) AND STANDARD DEVIATION (STD)

The consistency of the noise in the collected data is evaluated using root mean square and standard deviation. RMS and STD quantify the magnitude and deviation, respectively, of the noise present in the collected data. RMS and STD of noise are calculated using equation 9 and 10

$$RMS = \sqrt{\frac{1}{MN}\sum_{i=1}^{M}\sum_{j=1}^{N} n_{ij}^2} \tag{9}$$

$$STD = \sqrt{\frac{1}{MN-1}\sum_{i=1}^{M}\sum_{j=1}^{N} [n_{ij} - \bar{n}]^2} \tag{10}$$

where M and N are the number of rows and columns in the image, n_{ij} is the noise magnitude at pixel (i, j) obtained following the equation 11 and $\bar{n}$ is the mean value of the noise given by equation 12.

$$n_{ij} = X_{ij} - R_{ij} \tag{11}$$

$$\bar{n} = \frac{1}{MN} \sum_{i=1}^{M} \sum_{j=1}^{N} n_{ij} \tag{12}$$

V. DATA COLLECTION

A. PHANTOM PREPARATION

Generally, the quality of MRI images is assessed through phantom images following the guidelines set by the American College of Radiology (ACR) magnetic resonance accreditation program (MRAP) [68]. The MRAP approved phantom used for MRI imaging may be obtained commercially [68]. The phantom is constructed using acrylate plastic, glass, and silicone rubber. The cylindrical phantom is 16.5cm long and 20.4cm in diameter [68].

The phantom is filled with 10 millimolar (mM) nickel chloride solution containing sodium chloride (45 mM) to simulate biological conductivity. The contrast vial contains 20 mM nickel chloride and 15 mM sodium chloride solution providing a difference in T1 and T2 (T1 & T2 are longitudinal and transverse relaxation times) values. Actual values of T1 and T2 depend on the field strength in use and the temperature of the phantom.

B. MAGNETIC RESONANCE IMAGING (MRI)

The ACR phantom [68] was scanned 16 times with identical scan parameters on a General Electric Medical Systems 3.0 Tesla MR750 scanner (Waukesha, WI, software version DV29.1) with a 32 channel receive-only head coil. Magnitude, phase, real, and imaginary image components were saved to a disk. A 2D T1-weighted spin-echo sequence was used, with 18 slices of thickness = 0.5 mm, spacing = 5.5 mm, field-of-view = 25 × 25 cm, acquisition matrix size = 128 × 128, output image matrix size = 256 × 256 (resolution = 0.98×0.98 mm), TR = 26 ms, TE = 13 ms, flip angle = 90°, bandwidth = 15.63 kHz, and extended dynamic range (32 bit number format).

C. NOISE VARIANCE OF MRI PHANTOM IMAGES

The ACR phantom consists of 18 slices and each slice was scanned 16 times. The reference images of each slice are then computed by averaging the 16 scanned images. The mean RMS and STD of 16 images for each slice are shown in Table 2. The noise for the phantom MR images is obtained by subtracting the reference images from the noisy ones and the RMS and STD are calculated following equations 9 and 10, respectively. Furthermore, the RMS and STD of every image for all slices are tabulated in Table 6 in Appendix A.

VI. RESULTS AND DISCUSSION

The presented pixel-wise thresholding based denoising method is tested on the MR images of a standard ACR approved phantom. The performance of the algorithm is evaluated both qualitatively and quantitatively by computing the reduction in noise, recovery of the structural information, and enhancement in the visual quality of the image, typically quantified by peak-signal-to-noise-ratio, structural similarity index, and contrast-to-noise-ratio, respectively. The qualitative denoising result of the MR images of the phantom captured at different scans are depicted in Figures 4, 5, and 6.

A. NOISE REMOVAL

The qualitative denoising result of slices 2, 8, and 10 are shown column wise in Figure 4. The first, second, and third columns in Figure 4 illustrate the noisy, denoised, and reference images, respectively. The noisy images and reference images are obtained by averaging 3 and 16 repetitive scans, respectively. It should be noted that the noisy images used are the average of three scans that include previous, current, and next scans. It can be seen from Figure 4 that the structures in the noisy image are blurred due to the presence of noise, whereas, it is clearly visible in the denoised images. Visually, the denoised images are quite similar to the reference images. Additionally, noisy, denoised, and reference images at different scan numbers of slices 3 and 13 are shown in Figure 5.

Quantitatively, the noise removal efficacy is evaluated by calculating the peak-signal-to-noise ratio of the denoised images with respect to the reference images. PSNR of the noisy and denoised images of all the slices are tabulated in Table 3. It can be seen from Table 3 that the PSNR of the denoised images increases significantly compared to the noisy images. This increase in PSNR justifies the visual quality enhancement of the denoised images.

B. VISUAL QUALITY ENHANCEMENT

The noisy, denoised, and reference images of slices 1, 7, and 16 are shown column wise in Figure 6. The noisy images displayed in the first column of Figure 6 have some distinct features highlighted inside the red elliptical area. However, the features are visually masked due to the presence of noise. The denoised images shown in the second column of Figure 6 reveal visually clear images and recover the features suppressed in the noisy images. It can be seen that the wedges, square array, and the bright spots in Figure 6b, 6e and 6h, respectively are now clearly visible in the denoised images. One can visually confirm that the retrieved features are exactly the same as seen in the reference images exhibited in the third column of Figure 6. This illustrates that the presented pixel-wise denoising method removes noise effectively while preserving the finer details in the image.

We measured the structural similarity index and contrast-to-noise ratio to quantify feature recovery and visual quality enhancement of the denoised MR images, respectively. Both the SSIM and CNR of the noisy and denoised images are calculated with respect to the reference images. Table 3 tabulates the SSIM and CNR of the noisy and denoised image of all slices. It can be seen that the SSIM values of denoised images are ≥ 0.95, whereas, the SSIM values of the noisy images are < 0.5. This illustrates that the denoised image recovers

almost all the structural information masked in the noisy image by the noise. Furthermore, CNR values of the denoised image increase by 3-4 times in comparison to the noisy images leading to visually clean images.

C. SCAN TIME REDUCTION

In general, the MR images are averaged over multiple scans to obtain a good quality image. These multiple scans are collected and averaged internally by the machine's algorithm. However, the acquisition of multiple scans takes a longer time and can introduce motion artifacts. Hence, it is important to reduce the scan time, which can be achieved by denoising the image after a few scans. The reference images depicted in Figures 4, 5 and 6 are obtained by averaging 16 repetitive scans. However, a similar quality image is achieved by denoising the averaged image of the three repetitive scans. It can be seen from Figure 4, 5, and 6 that the denoised images are visually similar to the reference images. Additionally, the SSIM value of ≥ 0.95 indicates that all the structural information is intact in the denoised images. It should be noted that the recording of the reference image consumes approximately 23 minutes and 24 seconds, whereas the averaged image of the first three scans takes 4 minutes and 38 seconds. Further, the presented pixel-wise denoising method requires around one second of time to denoise the MR image. Hence, by utilizing the presented method the MRI scanning time can be made 2-3 times faster.

D. COMPARISON WITH EXISTING METHODS

We compared the performance of the presented pixel-wise thresholding method with the adaptive fuzzy hexagonal bilateral (AFHB) [28], Pre-smooth non-local means (PSNLM) [59], standard bilateral [25], and non-local means [53] filtering-based MRI denoising techniques. The noisy images obtained by averaging three repetitive scans are used to compare the performance of the above mentioned methods. Figure 7 depicts the comparison result of the MR images for adaptive bilateral filtering, PSNLM, and the presented pixel-wise denoising method. The first column of Figure 7 shows the noisy images of slices 1, 7, and 16. The second, third, and fourth columns of Figure 7 demonstrate the denoised images obtained from adaptive bilateral filtering, PSNLM filtering, and the presented pixel-wise denoising method, respectively. It can be seen from the second and third columns of figure 7 that the adaptive bilateral and PSNLM filtering successfully removes noise. However, the filtering methods failed to recover features inside the highlighted region. In fact, the unclear features inside the highlighted area of the noisy images are distorted due to the filtering operation. Both the adaptive bilateral and PSNLM filtering methods provide even poorer structural information in comparison to the noisy images. This can be confirmed from Figure 7, where the structures or square blocks hidden in the noisy images in the first column are filtered out in the denoised images seen in the second and third columns. The comparison results of the presented pixel-wise denoising method with the standard bilateral and non-local means filtering techniques shown in figure 8 in Appendix A illustrate the superior performance of the pixel-wise threshold selection method.

Table 4 tabulates the quantitative results of the presented pixel-wise denoising method, adaptive bilateral, and PSNLM filtering techniques. Both the filtering methods display a small improvement in PSNR compared to the noisy image, whereas the SSIM value is

similar to that of the noisy image. This illustrates that the filtering methods suppress the structural information present in the noisy image. Further, it can be seen from Table 3 that the CNR for both the adaptive bilateral and PSNLM filtering methods is significantly greater than that for the noisy images. However, a multi-fold increase in CNR value is observed for the presented pixel-wise denoising method. Similar comparative results are obtained for the standard bilateral and non-local means filtering techniques. The quantitative results are depicted in Table 7 in Appendix A.

1) EFFICIENCY COMPARISON—The CPU processing time and memory usage for an Intel Core i5-9300H CPU @ 2.40GHz with 32.0 GB installed RAM system is calculated for all three methods. It can be seen from Table 5 that the presented pixel-wise denoising method takes less than one second and uses approximately 128 MBs, respectively to execute denoising, whereas, the PSNLM filtering techniques take more than six seconds and use greater memory to complete the denoising process. The adaptive bilateral filtering takes a longer time and utilizes less memory to complete the denoising process.

VII. CONCLUSION

In this paper, we presented an SVD based pixel-wise threshold selection MRI denoising method. Unlike the truncated SVD denoising methods which utilize global thresholding, we perform pixel-wise thresholding of singular vectors. Qualitatively, the denoised image has improved visual quality and recovers suppressed features. The PSNR of the denoised image improves significantly, whereas, an SSIM of ≥ 0.95 demonstrates that the denoised image recovers all the structural information. A multi-fold increase in the CNR value illustrates enhancement in the image visual quality. Additionally, the presented pixel-wise denoising denoising method enables 2-3 times faster acquisition by denoising images of just the first few scans. Thus, the presented pixel-wise denoising method outperforms the widely used filtering methods in all quantitative parameters and takes lower CPU time to denoise. This technique can be integrated into magnetic resonance imaging systems to reduce acquisition time without compromising image quality.

ACKNOWLEDGMENT

Nimesh Srivastava would like to thank the program authors of the bilateral and NLM filtering algorithm, for making their code free and accessible for research purposes. The codes can be found at Non-Local Means: (https://www.mathworks.com/matlabcentral/fileexchange/52018-simple-non-local-means-nlm-filter) and Bilateral Filter: (https://www.mathworks.com/matlabcentral/fileexchange/12191-bilateral-filtering).

This work was supported in part by the National Institute of General Medical Sciences/National Institutes of Health under Grant R24GM146107, Grant R35GM151218, and Grant R35GM148272; and in part by the National Science Foundation under Grant 2044599.

Biographies

NIMESH SRIVASTAVA received the B.Tech. degree in electronics and communication engineering from Manipal Institute of Technology, Manipal, in 2020. He is currently pursuing M.S. degree with the Department of Chemistry and Chemical Biology, Cornell University.

He co-founded EZ Diagnostics Inc., in 2022, and has been the CEO of EZ Diagnostics Inc., since 2023. He was involved in a summer internship with the Central Electronics Engineering Research Institute, Pilani, India, in 2018. From 2019 to 2020, he was a Research Intern with the Department of Chemistry and Chemical Biology, Cornell University. In 2022, he was a Research Intern with the UCSF Medical Center. In 2023, he was a Research Intern with Weill-Cornell Medicine. His research interests include signal processing, image processing, magnetic resonance, and medical imaging diagnostics.

GYANA RANJAN SAHOO received the B.Sc. degree from the S.V.M. College, Utkal University, in 2011, the M.Sc. degree from the Department of Physics, Utkal University, Bhubaneswar, India, in 2013, and the Ph.D. degree in physics from Indian Institute of Technology Kanpur, India, in 2020.

From 2020 to 2021, he was a Research Assistant with the Department of Physics, Indian Institute of Technology Kanpur. Since 2021, he has been a Postdoctoral Research Associate with the Department of Chemistry and Chemical Biology, Cornell University, Ithaca, NY, USA. His research interests include signal processing, wavelet analysis, image segmentation, machine learning, optical spectroscopy, and imaging diagnostics.

Dr. Sahoo is a member of Society of Photographic Instrumentation Engineers (SPIE) and was General Secretary of IIT Kanpur Student Chapter of the Optical Society of America (OSA), from September 2017 to October 2018. He is also the Co-Founder of PhotoSpIMeDx Pvt. Ltd., in 2019, and was the CTO of PhotoSpIMeDx Pvt. Ltd., until 2022.

HENNING U. VOSS received the Diploma and Ph.D. degrees in physics from Potsdam University, in 1994 and 1998, respectively. He studied physics in Hamburg and Potsdam, Germany. He is currently the Director of the Cornell MRI Facility, Ithaca, NY, USA. Since 2009, he has been an Associate Professor in physics and in radiology with Weill Cornell Medicine, New York City. From 2000 to 2003, he was an Assistant Professor with Freiburg University, Germany. From 2003 to 2009, he was an Assistant Professor in physics and in

radiology with Freiburg University. His publications include articles in IEEE TRANSACTIONS ON MEDICAL IMAGING, IEEE TRANSACTIONS ON BIOMEDICAL ENGINEERING, and IEEE ACCESS. His research interests include imaging techniques, modeling and control of dynamical systems, and applications of these fields to biomedical research in general and to the neurosciences in particular. He is a member of the International Society for Magnetic Resonance in Medicine. He is an Awardee of the Otto Hahn Medal of the Max Planck Society.

SUMIT N. NIOGI received the B.A. degree in physics and in mathematics from the University of Pennsylvania, in 2001, and the Ph.D. degree in physiology, biophysics, and systems biology and the M.D. degree in medicine from the Joan & Sanford I Weill Medical College, Cornell University, in 2007 and 2010, respectively.

He was a Surgery Intern and a Radiology Resident and Neuroradiology Fellow with the Weill Cornell Medical College, from 2010 to 2011, from 2011 to 2015, and from 2015 to 2016, respectively. In 2016, he accepted a faculty member position with the Department of Radiology, Weill Cornell Medicine, where he is currently an Assistant Professor in radiology. He is currently the Executive Director of Cornell University MRI Facility and the Director of the Imaging Data Evaluation & Analysis Laboratory. His research interests include magnetic resonance diffusion tensor imaging, mild traumatic brain injury, and neurodegenerative disease.

Dr. Niogi is a member of American Society of Neuroradiology, the Radiology Society of North America, American College of Radiology, New York Roentgen Ray Society, American Roentgen Ray Society, and the International Society for Magnetic Resonance in Medicine. He was a recipient of the DuVigneaud Research Symposium First Year Award, in 2003, the DuVigneaud Research Symposium Award of Excellence, in 2005, the International Society for Magnetic Resonance in Medicine Educational Award, in 2007, and the Roentgen Resident Research Award by the Radiological Society of North America, in 2014.

JACK H. FREED received the B.E. degree in chemical engineering from Yale University, New Haven, CT, USA, in 1958, and the M.S. and Ph.D. degrees in chemistry from Columbia University, New York City, NY, USA, in 1959 and 1962, respectively.

He was a Postdoctoral Fellow with the University of Cambridge, Cambridge, U.K., from 1962 to 1963. In 1963, he accepted a Faculty Appointment with Cornell University, Ithaca, NY, USA, where he has spent his subsequent career as an Assistant Professor,

from 1963 to 1967, an Associate Professor, from 1967 to 1973, a Professor, from 1973 to 2016, an Emeritus, since 2016, and has been a Frank and Robert Laughlin Professor in physical chemistry, since 2007. He has been the Director of the National Biomedical Center for Advanced ESR Technology, since 2001. He has also held positions as a Visiting Scientist with U.S. Japan Cooperative Science Program, Tokyo University, Japan, in 1969; a Guest Professor with Aarhus University, Denmark, in 1974; a Visiting Professor with the University of Geneva, Switzerland, in 1977; a Visiting Professor with Delft University of Technology, The Netherlands, in 1978, l'École Normale Supérieure, Paris, France (1984–1985), and the University of Padua, Italy, in 1991; a Charles A. MacDowell Lecturer in chemical physics with the University of British Columbia, in 1997; a Distinguished Visiting Professor with Yamagata University, Japan, in 1998; a Visiting Scientist with the University of Oxford, U.K. (2007–2013); and an Israel Pollak Distinguished Lecturer with the Technion, Israel, in 2009. He has authored over 400 publications and holds several patents. His research interests include the development of modern technology for electron-spin resonance (ESR) spectroscopy both in the development of modern spectrometers and in the theoretical interpretation of ESR experiments designed to elucidate the structural dynamics of complex fluids, such as liquid crystals and membranes and the structure/function of membrane proteins and protein complexes.

Prof. Freed is a fellow of American Physical Society, in 1976, American Academy of Arts and Sciences, in 1994, the Royal Society of Chemistry, in 2009, and American Association for the Advancement of Science, in 2009. He has also been an Honorary U.S. Ramsay Memorial Fellow (1962–1963); an NSF Postdoctoral Fellow with Cambridge University (1962–1963); an A. P. Sloan Foundation Fellow (1966–1968); the Weizmann Institute of Science Senior Fellow, in 1970; a John Simon Guggenheim Memorial Fellow (1984–1985), the Institute for Advanced Studies, The Hebrew University of Jerusalem, in 1990; and an Inaugural Fellow of the International Society of Magnetic Resonance, in 2008. In 2001, he became a Honorary Member of the National Magnetic Resonance Society of India. Since 2006, he has been on the external advisory board of the National High Magnetic Field Laboratory, USA. He has served on many journal editorial boards, including *The Journal of Chemical Physics* (1976–1978), the *The Journal of Physical Chemistry* (1979–1983), *Chemical Physics Letters* (1988–1990), *Applied Magnetic Resonance* (1990–2016), and *Magnetic Resonance Review* (1994–2000); and was an Associate Editor of the *Journal of Magnetic Resonance* (2007–2010). He chaired the Gordon Research Conference on Magnetic Resonance, in 1975. From 2008 to 2010, he was the President of the International EPR/ESR Society. Among his awards are the BuckWhitney Award in Pure and Applied Chemistry, in 1981, by American Chemical Society (ACS); the Bruker Award in ESR by the Royal Society of Chemistry, in 1990; the International Electron Spin Resonance Society Gold Medal, in 1994; the Irving Langmuir Prize in Chemical Physics by American Physical Society, in 1997; the Zavoisky Prize, in 1998, in ESR and the Voevodski Prize, in 2017; by Russian Academy of Sciences; the E. Bright Wilson Award in Spectroscopy by the ACS, in 2008; the ISMAR Prize from the International Society of Magnetic Resonance, in 2013; the Joel H. Hildebrand Award in the Chemistry of Liquids by the ACS, in 2014; and the Richard Ernst Prize by EUROMAR, in 2023. In honor of his extensive achievements, the *Journal*

of Physical Chemistry issued a special J. H. Freed Festschrift Issue, in 2004, on his 65th birthday.

MADHUR SRIVASTAVA (Member, IEEE) received the B.Tech. degree in electronics and communication engineering from the Jaypee University of Engineering and Technology (JUET), Guna, India, in 2011, and the M.Eng. degree in electrical and computer engineering and the M.S. and Ph.D. degrees in biomedical engineering from Cornell University, Ithaca, NY, USA, in 2012, 2016, and 2018, respectively.

In 2019, he accepted a faculty member position with the Department of Chemistry and Chemical Biology, Cornell University, where is currently an Assistant Research Professor. He has been a Visiting Scholar with the Medical Research and Clinical Practice Program, Weill Cornell Medicine, in 2015; the Geisel School of Medicine, Dartmouth College, in 2017; the Department of Chemistry, University of California at Santa Barbara, in 2018; the Citigroup Biomedical Imaging Center, Weill Cornell Medicine, in 2018; the National Cancer Institute, National Institutes of Health, in 2019; and the Department of Radiology, Weill Cornell Medicine, in 2019. His research interests include signal and image processing and magnetic resonance spectroscopy and imaging.

Dr. Srivastava is a member of the International Electron Paramagnetic Resonance Society, the Biophysical Society, American Chemical Society, the International Society of Magnetic Resonance, and New YorkAcademy of Sciences; and was a Student Member of the Institution of Electronics and Telecommunications Engineers (2007–2011). He was a Nominated Member of the Clinton Global Initiative University (2017–2019). He was a recipient of the Certificate of Merit at JUET, in 2010, the Ericsson's University Relationship Program (EMPOWER) Fellowship-India, in 2010, the Summer Research Fellowship from Indian Institute of Science Education and Research-Kolkata, India, in 2010, the Vice-Chancellor's Gold Medal from JUET, in 2011, the Ph.D. Technology Commercialization Fellowship from Cornell University, in 2016, where he was with the Graduate School Research Grant, in 2017, the Electron Spin Resonance Technology Transfer Experience Award by SharedEPR (2017 and 2018), the Alumni Association Academic Enrichment Grant from Cornell University, in 2017, where he was with the Phool Prakash and Rukmini Sahai Graduate Fellowship, in 2017, the Clinton Global Initiative-University Pitch Competition Award, in 2018, and the Cornell Technology Acceleration and Maturation Award at Cornell University, in 2019. He was the Finalist of the NIH Director's Early Independence Award, in 2019, and the Bruker ESR Thesis Prize by Royal Society of Chemistry, in 2019. During the Ph.D. studies, he was also a recipient of many conference travel grants: the Graduate School, Cornell University (2016 and 2017); the 58th Rocky Mountain Conference on Magnetic Resonance, in 2016; the Entrepreneurship@Cornell, Cornell University, in 2017; the Office of Engagement Initiatives, Cornell University,

in 2017; the International Conference on EPR Spectroscopy and Imaging of Biological Systems, in 2017; and the 20th International Society of Magnetic Resonance Meeting, in 2017.

APPENDIX A

Figure 8 shows the comparative denoising results of PWT with Bilateral and Non-local means filtering. The first column of Figure 8 shows the noisy images of slices 1, 7, and 16. The second, third, and fourth columns of Figure 8 demonstrate the denoised images obtained from bilateral filtering, NLM filtering, and the presented pixel-wise denoising method, respectively.

REFERENCES

[1]. Mohan J, Krishnaveni V, and Guo Y, "A survey on the magnetic resonance image denoising methods," Biomed. Signal Process. Control, vol. 9, pp. 56–69, Jan. 2014.

[2]. Mohsen YM, Abdelghany HS, and Saleh RN, "Advanced magnetic resonance imaging (MRI) technique (double inversion recovery sequence) in the diagnosis of multiple sclerosis (MS) grey matter lesions," Minia J. Med. Res, vol. 34, no. 1, pp. 65–75, 2023.

[3]. Henkelman RM, "Measurement of signal intensities in the presence of noise in MR images," Med. Phys, vol. 12, no. 2, pp. 232–233, Mar. 1985. [PubMed: 4000083]

[4]. Gudbjartsson H and Patz S, "The Rician distribution of noisy mri data," Magn. Reson. Med, vol. 34, no. 6, pp. 910–914, Dec. 1995. [PubMed: 8598820]

[5]. Dietrich O, Raya JG, Reeder SB, Reiser MF, and Schoenberg SO, "Measurement of signal-to-noise ratios in MR images: Influence of multichannel coils, parallel imaging, and reconstruction filters," J. Magn. Reson. Imag, vol. 26, no. 2, pp. 375–385, Aug. 2007.

[6]. Dietrich O, Raya JG, Reeder SB, Ingrisch M, Reiser MF, and Schoenberg SO, "Influence of multichannel combination, parallel imaging and other reconstruction techniques on MRI noise characteristics," Magn. Reson. Imag, vol. 26, no. 6, pp. 754–762, Jul. 2008.

[7]. Cheng G, Lang C, and Han J, "Holistic prototype activation for few-shot segmentation," IEEE Trans. Pattern Anal. Mach. Intell, vol. 45, no. 4, pp. 4650–4666, Apr. 2023. [PubMed: 35877806]

[8]. Lang C, Cheng G, Tu B, Li C, and Han J, "Base and meta: A new perspective on few-shot segmentation," IEEE Trans. Pattern Anal. Mach. Intell, vol. 45, no. 9, pp. 10669–10686, Apr. 2023. [PubMed: 37037231]

[9]. Lang C, Cheng G, Tu B, and Han J, "Few-shot segmentation via divide- and-conquer proxies," Int. J. Comput. Vis, vol. 132, no. 1, pp. 261–283, Jan. 2024.

[10]. Lang C, Wang J, Cheng G, Tu B, and Han J, "Progressive parsing and commonality distillation for few-shot remote sensing segmentation," IEEE Trans. Geosci. Remote Sens, vol. 61, 2023, Art. no. 5613610.

[11]. Sahoo GR, Jagtap J, Panigrahi P, Pradhan A, and Srivastava M, "Adaptive image quantization for discrimination of cervical pre-cancer," Proc. SPIE, vol. 13006, pp. 217–225, Jun. 2024.

[12]. Singh P, Sahoo GR, and Pradhan A, "Spatio-temporal map for early cancer detection: Proof of concept," J. Biophotonics, vol. 11, no. 8, Aug. 2018, Art. no. e201700181. [PubMed: 29411946]

[13]. Srivastava M and Freed JH, "Singular value decomposition method to determine distance distributions in pulsed dipolar electron spin resonance," J. Phys. Chem. Lett, vol. 8, no. 22, pp. 5648–5655, Nov. 2017. [PubMed: 29099190]

[14]. Srivastava M and Freed JH, "Singular value decomposition method to determine distance distributions in pulsed dipolar electron spin resonance: II. Estimating uncertainty," J. Phys. Chem. A, vol. 123, no. 1, pp. 359–370, Jan. 2019. [PubMed: 30525624]

[15]. McVeigh ER, Henkelman RM, and Bronskill MJ, "Noise and filtration in magnetic resonance imaging," Med. Phys, vol. 12, no. 5, pp. 586–591, Sep. 1985. [PubMed: 4046992]

[16]. Perona P and Malik J, “Scale-space and edge detection using anisotropic diffusion,” IEEE Trans. Pattern Anal. Mach. Intell, vol. 12, no. 7, pp. 629–639, Jul. 1990.

[17]. Krissian K and Aja-Fernandez S, “Noise-driven anisotropic diffusion filtering of MRI,” IEEE Trans. Image Process, vol. 18, no. 10, pp. 2265–2274, Oct. 2009. [PubMed: 19546041]

[18]. Samsonov AA and Johnson CR, “Noise-adaptive nonlinear diffusion filtering of MR images with spatially varying noise levels,” Magn. Reson. Med, vol. 52, no. 4, pp. 798–806, Oct. 2004. [PubMed: 15389962]

[19]. Tong C, Sun Y, Payet N, and Ong S-H, “A general strategy for anisotropic diffusion in MR image denoising and enhancement,” Magn. Reson. Imag, vol. 30, no. 10, pp. 1381–1393, Dec. 2012.

[20]. Srivastava A, Bhateja V, and Tiwari H, “Modified anisotropic diffusion filtering algorithm for MRI,” in Proc. 2nd Int. Conf. Comput. Sustain. Global Develop. (INDIACom), Mar. 2015, pp. 1885–1890.

[21]. Joshi N and Jain S, “An improved anisotropic diffusion filtering approach for noise reduction in MRI,” in Proc. 9th Int. Conf. Rel., INFOCOM Technol. Optim., Trends Future Direction (ICRITO), Sep. 2021, pp. 1–5.

[22]. Pal C, Das P, Chakrabarti A, and Ghosh R, “Rician noise removal in magnitude MRI images using efficient anisotropic diffusion filtering,” Int. J. Imag. Syst. Technol, vol. 27, no. 3, pp. 248–264, Sep. 2017.

[23]. Walker SA, Miller D, and Tanabe J, “Bilateral spatial filtering: Refining methods for localizing brain activation in the presence of parenchymal abnormalities,” NeuroImage, vol. 33, no. 2, pp. 564–569, Nov. 2006. [PubMed: 16942890]

[24]. Xie J, Heng P-A, and Shah M, “Image diffusion using saliency bilateral filter,” IEEE Trans. Inf. Technol. Biomed, vol. 12, no. 6, pp. 768–771, Nov. 2008. [PubMed: 19000957]

[25]. Hamarneh G and Hradsky J, “Bilateral filtering of diffusion tensor magnetic resonance images,” IEEE Trans. Image Process, vol. 16, no. 10, pp. 2463–2475, Oct. 2007. [PubMed: 17926929]

[26]. Akdemir Akar S, “Determination of optimal parameters for bilateral filter in brain MR image denoising,” Appl. Soft Comput, vol. 43, pp. 87–96, Jun. 2016.

[27]. Chang H-H, Chiang M-C, Sheu TWH, and Huang H, “A contrast-enhanced trilateral filter for MR image denoising,” in Proc. IEEE Int. Symp. Biomed. Imag., Nano Macro, Mar. 2011, pp. 1823–1826.

[28]. Kala R and Deepa P, “Adaptive fuzzy hexagonal bilateral filter for brain MRI denoising,” Multimedia Tools Appl, vol. 79, nos. 21–22, pp. 15513–15530, Jun. 2020.

[29]. Nowak RD, “Wavelet-based Rician noise removal for magnetic resonance imaging,” IEEE Trans. Image Process, vol. 8, no. 10, pp. 1408–1419, Oct. 1999. [PubMed: 18267412]

[30]. Pizurica A, Philips W, Lemahieu I, and Acheroy M, “A versatile wavelet domain noise filtration technique for medical imaging,” IEEE Trans. Med. Imag, vol. 22, no. 3, pp. 323–331, Mar. 2003.

[31]. Bao P and Zhang L, “Noise reduction for magnetic resonance images via adaptive multiscale products thresholding,” IEEE Trans. Med. Imag, vol. 22, no. 9, pp. 1089–1099, Sep. 2003.

[32]. Luisier F, Blu T, and Wolfe PJ, “A CURE for noisy magnetic resonance images: Chi-square unbiased risk estimation,” IEEE Trans. Image Process, vol. 21, no. 8, pp. 3454–3466, Aug. 2012. [PubMed: 22491082]

[33]. Gupta D and Ahmad M, “Brain MR image denoising based on wavelet transform,” Int. J. Adv. Technol. Eng. Explor, vol. 5, no. 38, pp. 11–16, Jan. 2018.

[34]. Ali MN, “A wavelet-based method for MRI liver image denoising,” Biomed. Eng./ Biomedizinische Technik, vol. 64, no. 6, pp. 699–709, Dec. 2019.

[35]. Yang X and Fei B, “A wavelet multiscale denoising algorithm for magnetic resonance (MR) images,” Meas. Sci. Technol, vol. 22, no. 2, Feb. 2011, Art. no. 025803.

[36]. Padmagireeshan SJ, Johnson RC, Balakrishnan AA, Paul V, Pillai AV, and Raheem AA, “Performance analysis of magnetic resonance image denoising using contourlet transform,” in Proc. 3rd Int. Conf. Adv. Comput. Commun, Aug. 2013, pp. 396–399.

[37]. Tsai K, Ma J, Ye D, and Wu J, “Curvelet processing of MRI for local image enhancement,” Int. J. Numer. Methods Biomed. Eng, vol. 28, nos. 6–7, pp. 661–677, Jun. 2012.

[38]. Biswas R, Purkayastha D, and Roy S, “Denoising of MRI images using curvelet transform,” in Advances in Systems, Control and Automation: ETAEERE-2016. Singapore: Springer, 2016, pp. 575–583.

[39]. He L and Greenshields IR, “A nonlocal maximum likelihood estimation method for Rician noise reduction in MR images,” IEEE Trans. Med. Imag, vol. 28, no. 2, pp. 165–172, Feb. 2009.

[40]. Rajan J, Jeurissen B, Verhoye M, Van Audekerke J, and Sijbers J, “Maximum likelihood estimation-based denoising of magnetic resonance images using restricted local neighborhoods,” Phys. Med. Biol, vol. 56, no. 16, pp. 5221–5234, Aug. 2011. [PubMed: 21791732]

[41]. Sudeep PV, Palanisamy P, Kesavadas C, and Rajan J, “An improved nonlocal maximum likelihood estimation method for denoising magnetic resonance images with spatially varying noise levels,” Pattern Recognit. Lett, vol. 139, pp. 34–41, Nov. 2020.

[42]. Rajan J, Veraart J, Van Audekerke J, Verhoye M, and Sijbers J, “Nonlocal maximum likelihood estimation method for denoising multiple-coil magnetic resonance images,” Magn. Reson. Imag, vol. 30, no. 10, pp. 1512–1518, Dec. 2012.

[43]. Aja-Fernandez S, Alberola-Lopez C, and Westin C-F, “Noise and signal estimation in magnitude MRI and Rician distributed images: A LMMSE approach,” IEEE Trans. Image Process, vol. 17, no. 8, pp. 1383–1398, Aug. 2008. [PubMed: 18632347]

[44]. Sudeep PV, Palanisamy P, Kesavadas C, and Rajan J, “Nonlocal linear minimum mean square error methods for denoising MRI,” Biomed. Signal Process. Control, vol. 20, pp. 125–134, Jul. 2015.

[45]. Golshan HM, Hasanzadeh RPR, and Yousefzadeh SC, “An MRI denoising method using image data redundancy and local SNR estimation,” Magn. Reson. Imag, vol. 31, no. 7, pp. 1206–1217, Sep. 2013.

[46]. López-Rubio E and Florentín-Núñez MN, “Kernel regression based feature extraction for 3D MR image denoising,” Med. Image Anal, vol. 15, no. 4, pp. 498–513, Aug. 2011. [PubMed: 21414834]

[47]. Wong A and Mishra AK, “Quasi-Monte Carlo estimation approach for denoising MRI data based on regional statistics,” IEEE Trans. Biomed. Eng, vol. 58, no. 4, pp. 1076–1083, Apr. 2011. [PubMed: 20442039]

[48]. Monir SMG and Siyal MY, “Denoising functional magnetic resonance imaging time-series using anisotropic spatial averaging,” Biomed. Signal Process. Control, vol. 4, no. 1, pp. 16–25, Jan. 2009.

[49]. Luo J, Zhu Y, and Magnin IE, “Denoising by averaging reconstructed images: Application to magnetic resonance images,” IEEE Trans. Biomed. Eng, vol. 56, no. 3, pp. 666–674, Mar. 2009. [PubMed: 19389683]

[50]. Luo J, Zhu Y, and Hiba B, “Medical image denoising using one-dimensional singularity function model,” Computerized Med. Imag. Graph, vol. 34, no. 2, pp. 167–176, Mar. 2010.

[51]. Joshi N, Jain S, and Agarwal A, “An improved approach for denoising MRI using non local means filter,” in Proc. 2nd Int. Conf. Next Gener. Comput. Technol. (NGCT), Oct. 2016, pp. 650–653.

[52]. Wu T, Xie L, and Peng B, “A magnetic resonance imaging denoising technique using non-local means and unsupervised learning,” Int. J. Inf. Commun. Technol, vol. 16, no. 2, p. 152, 2020.

[53]. Gal Y, Mehnert AJH, Bradley AP, McMahon K, Kennedy D, and Crozier S, “Denoising of dynamic contrast-enhanced MR images using dynamic nonlocal means,” IEEE Trans. Med. Imag, vol. 29, no. 2, pp. 302–310, Feb. 2010.

[54]. Liu H, Yang C, Pan N, Song E, and Green R, “Denoising 3D MR images by the enhanced non-local means filter for Rician noise,” Magn. Reson. Imag, vol. 28, no. 10, pp. 1485–1496, Dec. 2010.

[55]. Hu J, Pu Y, Wu X, Zhang Y, and Zhou J, “Improved DCT-based nonlocal means filter for MR images denoising,” Comput. Math. Methods Med, vol. 2012, pp. 1–14, Jan. 2012.

[56]. Manjón JV, Coupé P, Martí-Bonmatí L, Collins DL, and Robles M, “Adaptive non-local means denoising of MR images with spatially varying noise levels,” J. Magn. Reson. Imag, vol. 31, no. 1, pp. 192–203, Jan. 2010.

[57]. Manjón JV, Coupé P, Buades A, Collins DL, and Robles M, “New methods for MRI denoising based on sparseness and self-similarity,” Med. Image Anal, vol. 16, no. 1, pp. 18–27, Jan. 2012. [PubMed: 21570894]

[58]. Coupé P, Manjón JV, Robles M, and Collins DL, “Adaptive multiresolution non-local means filter for three-dimensional magnetic resonance image denoising,” IET Image Process, vol. 6, no. 5, p. 558, 2012.

[59]. Yang J, Fan J, Ai D, Zhou S, Tang S, and Wang Y, “Brain MR image denoising for Rician noise using pre-smooth non-local means filter,” Biomed. Eng. OnLine, vol. 14, no. 1, pp. 1–20, Dec. 2015. [PubMed: 25564100]

[60]. Manjon J, Carbonellcaballero J, Lull J, Garciamarti G, Martibonmati L, and Robles M, “MRI denoising using non-local means,” Med. Image Anal, vol. 12, no. 4, pp. 514–523, Aug. 2008. [PubMed: 18381247]

[61]. Manjón JV, Coupé P, and Buades A, “MRI noise estimation and denoising using non-local PCA,” Med. Image Anal, vol. 22, no. 1, pp. 35–47, May 2015. [PubMed: 25725303]

[62]. Dabov K, Foi A, Katkovnik V, and Egiazarian K, “Image denoising by sparse 3-D transform-domain collaborative filtering,” IEEE Trans. Image Process, vol. 16, no. 8, pp. 2080–2095, Aug. 2007. [PubMed: 17688213]

[63]. Tripathi PC and Bag S, “CNN-DMRI: A convolutional neural network for denoising of magnetic resonance images,” Pattern Recognit. Lett, vol. 135, pp. 57–63, Jul. 2020.

[64]. El Zein M, El Laz W, Laza M, Wazzan T, Kaakour I, Adla YA, Baalbaki J, Diab MO, Sabbah M, and Zantout R, “A deep learning framework for denoising MRI images using autoencoders,” in Proc. BioSMART, Jun. 2023, pp. 1–4.

[65]. Guo Q, Zhang C, Zhang Y, and Liu H, “An efficient SVD-based method for image denoising,” IEEE Trans. Circuits Syst. Video Technol, vol. 26, no. 5, pp. 868–880, May 2016.

[66]. Gavish M and Donoho DL, “The optimal hard threshold for singular values is 4/3,” IEEE Trans. Inf. Theory, vol. 60, no. 8, pp. 5040–5053, Oct. 2014.

[67]. Wang Z, Bovik AC, Sheikh HR, and Simoncelli EP, “Image quality assessment: From error visibility to structural similarity,” IEEE Trans. Image Process, vol. 13, no. 4, pp. 600–612, Apr. 2004. [PubMed: 15376593]

[68]. American College of Radiology. (Apr. 2018). Phantom Test Guidance for Use of the Small MRI Phantom for American College of Radiology. [Online]. Available: https://www.acraccreditation.org/-/media/ACRAccreditation/Documents/MRI/SmallPhantomGuidance.pdf

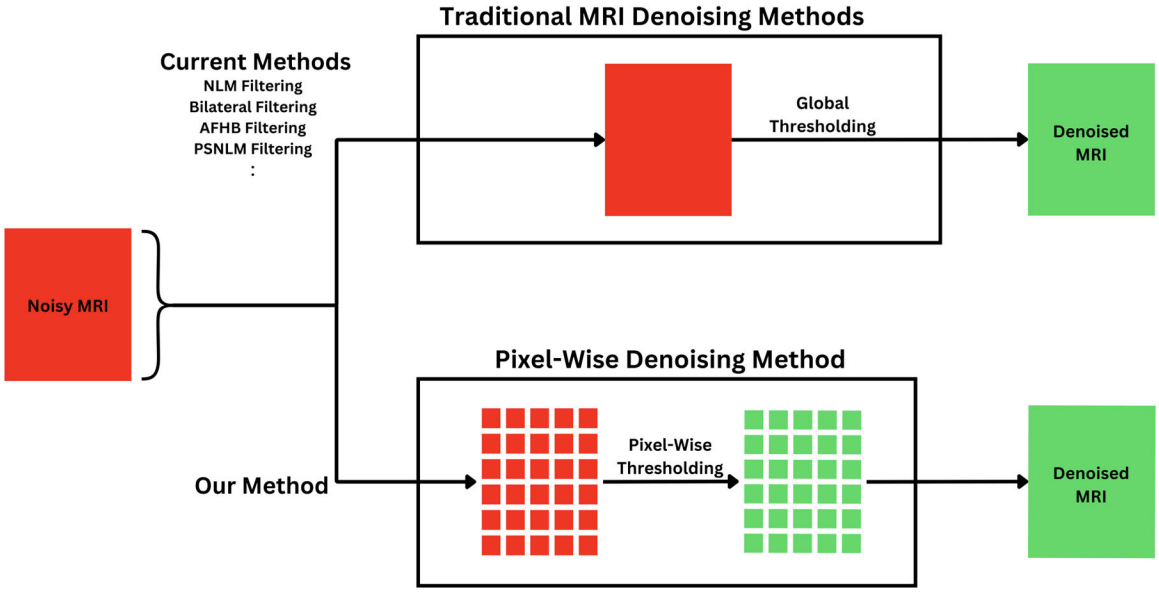

FIGURE 1.

Flowchart of current denoising methods vs presented pixel-wise denoising method. AFHB: Adaptive fuzzy hexagonal bilateral, PSNLM: Pre-smooth non-local means.

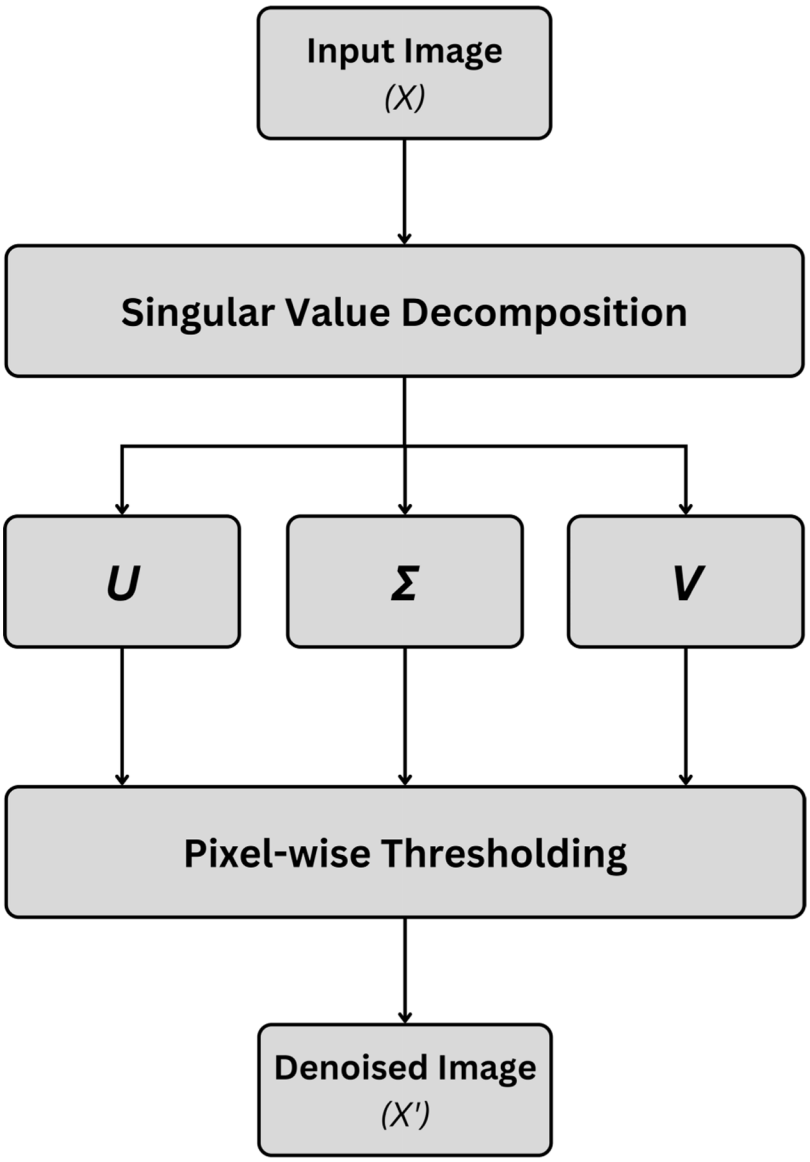

FIGURE 2.
Flowchart of the presented pixel-wise thresholding (PWT) method.

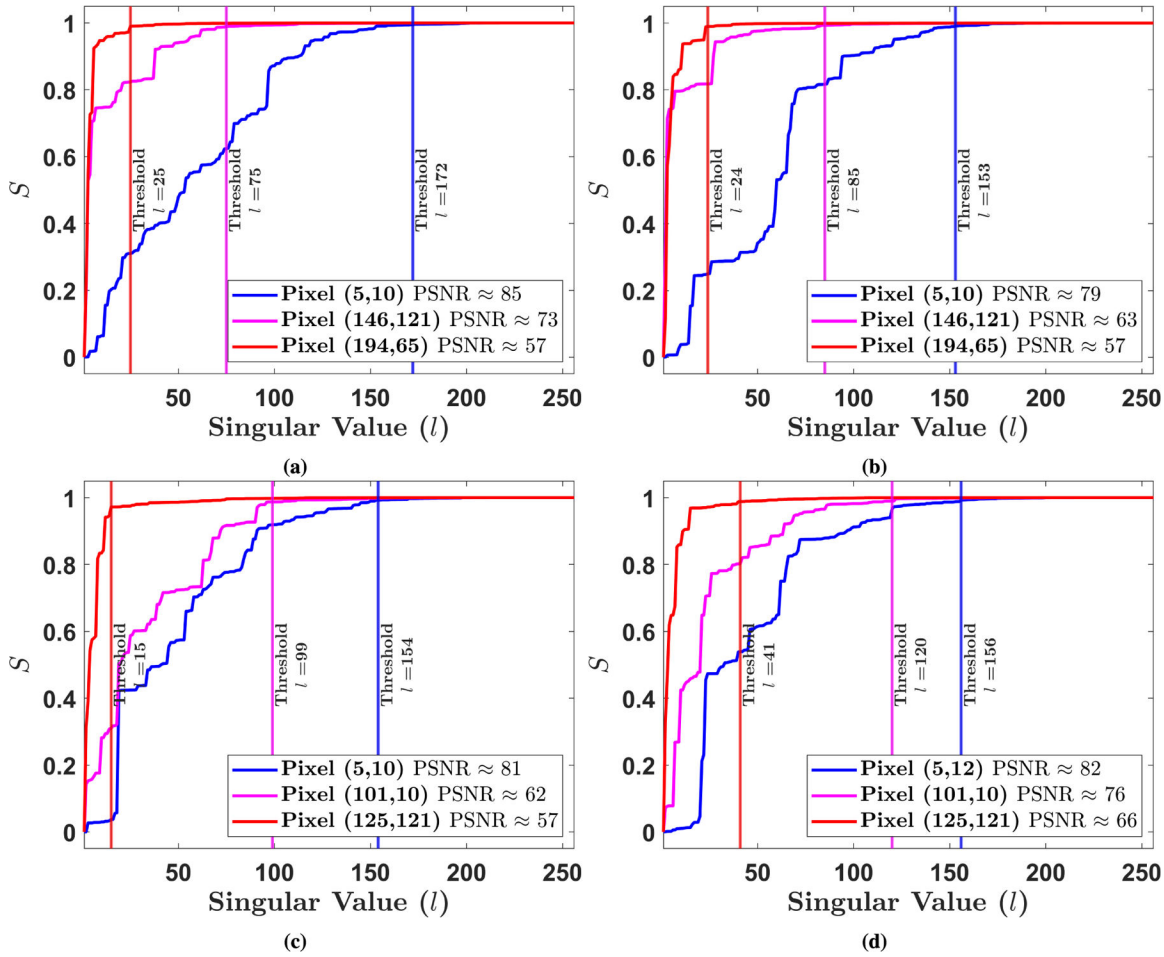

FIGURE 3.

Plot of *S* vs *l* at different pixels for images of (a) Slice-1, (b) Slice-2, (c) Slice-3, and (d) Slice-4. *S* at different pixels saturate at different singular values depending on the PSNR of that pixel. The vertical lines belong to the threshold singular value.

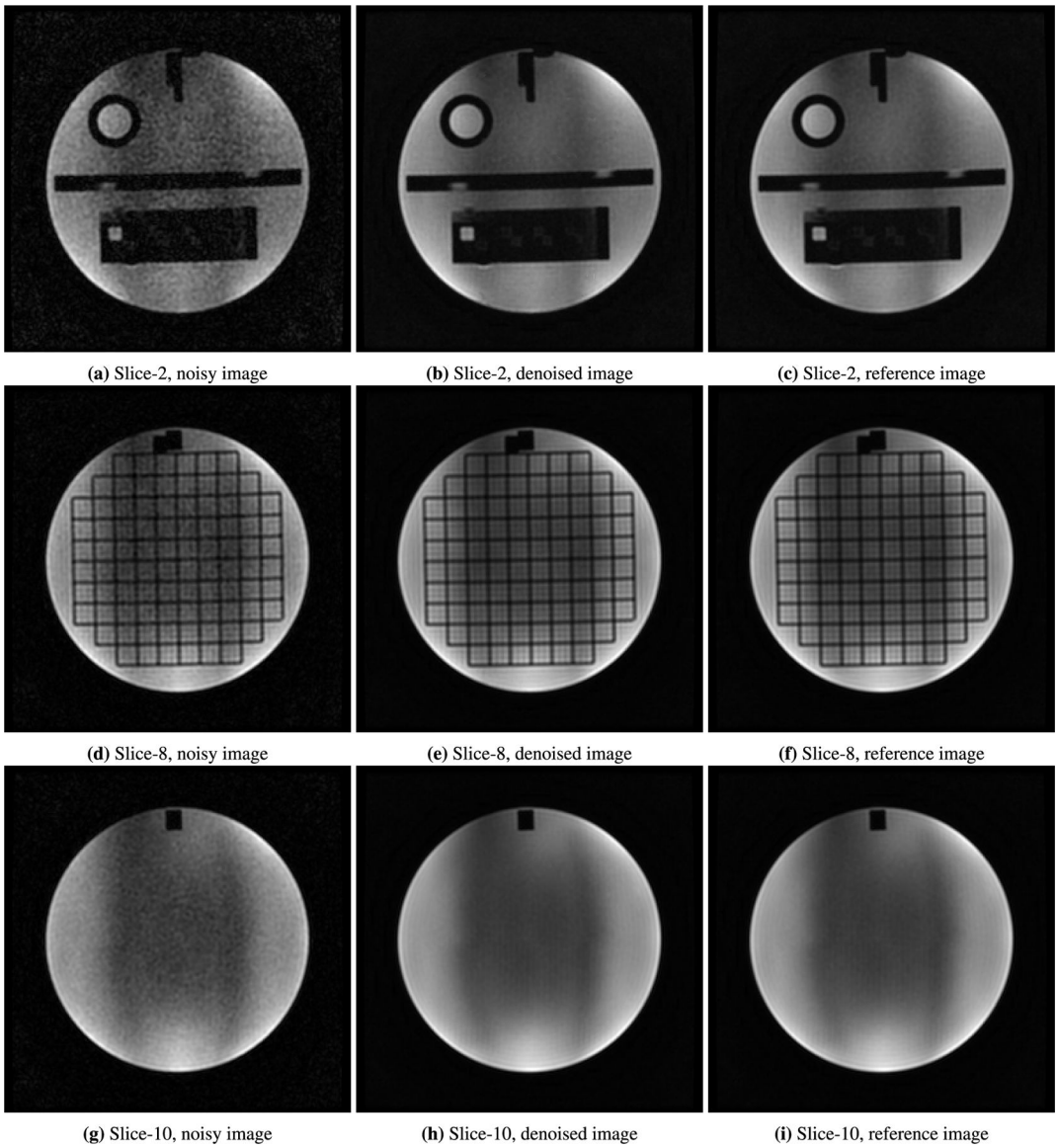

FIGURE 4.

Denoising results of MRI scan of the ACR phantom for slices 2 (first row), 8 (second row), and 10 (third row) respectively. The noisy and reference images are obtained after averaging 3 and 16 identical scans respectively. The denoised images display improved image quality and enhanced visibility.

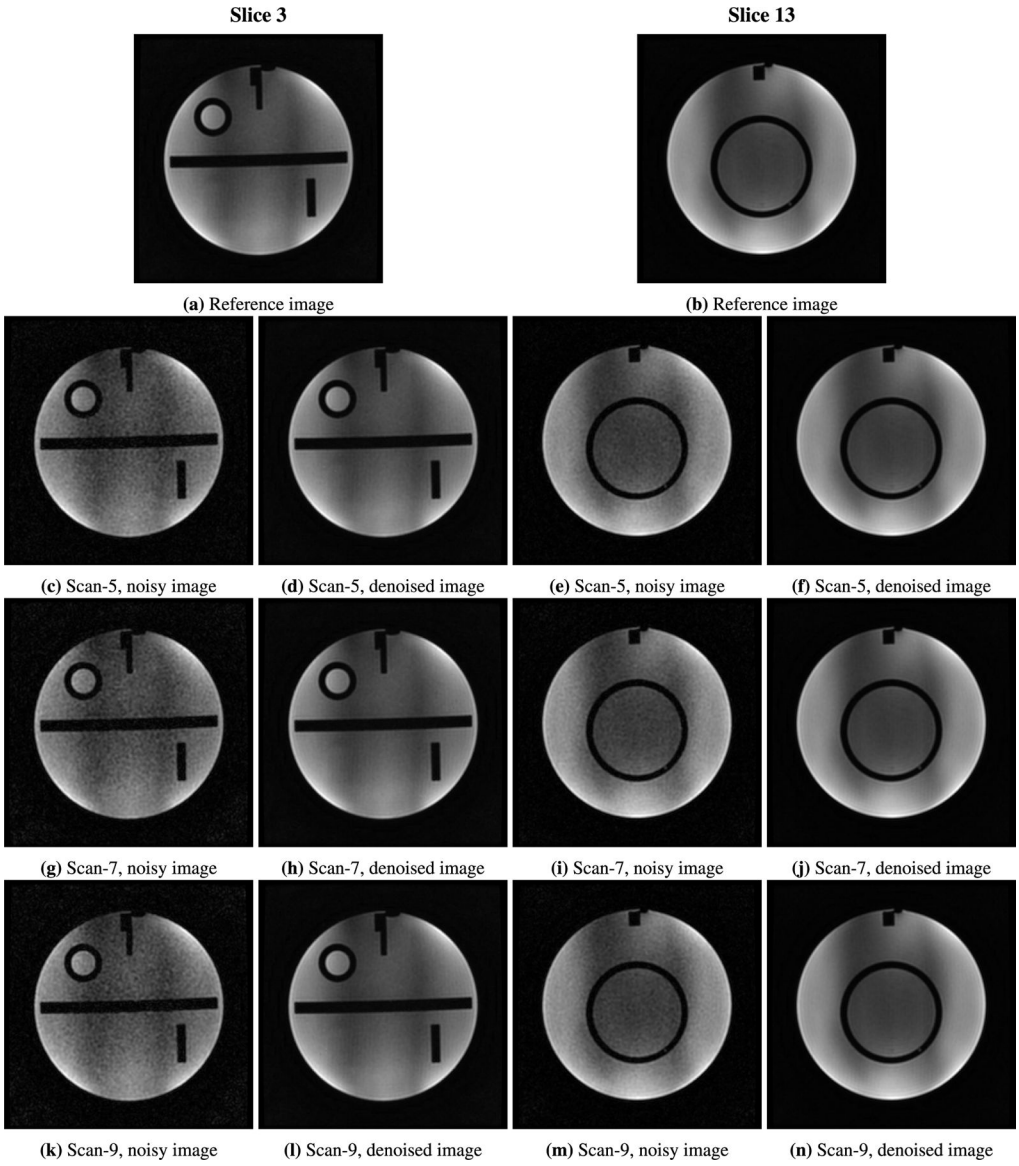

FIGURE 5.

Denoising results of MRI scans of ACR Phantom for slices 3 and 13 at scan numbers 5,7, and 9, respectively. The results are consistent across different scans.

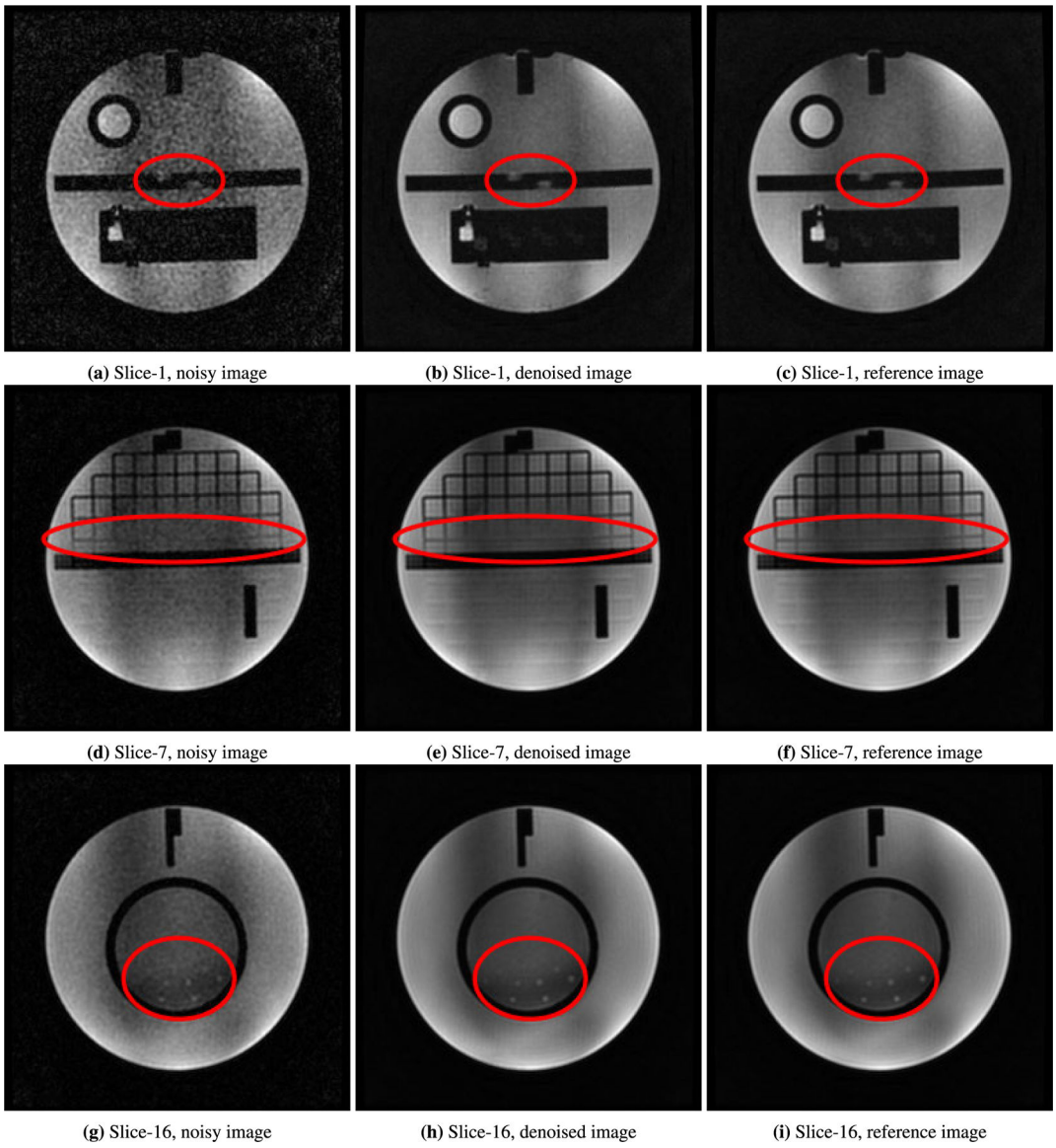

FIGURE 6.

Denoising results of MRI scan of the ACR phantom for slices 1,7 and 16 respectively. The highlighted area in the figure illustrates the recovered features after denoising.

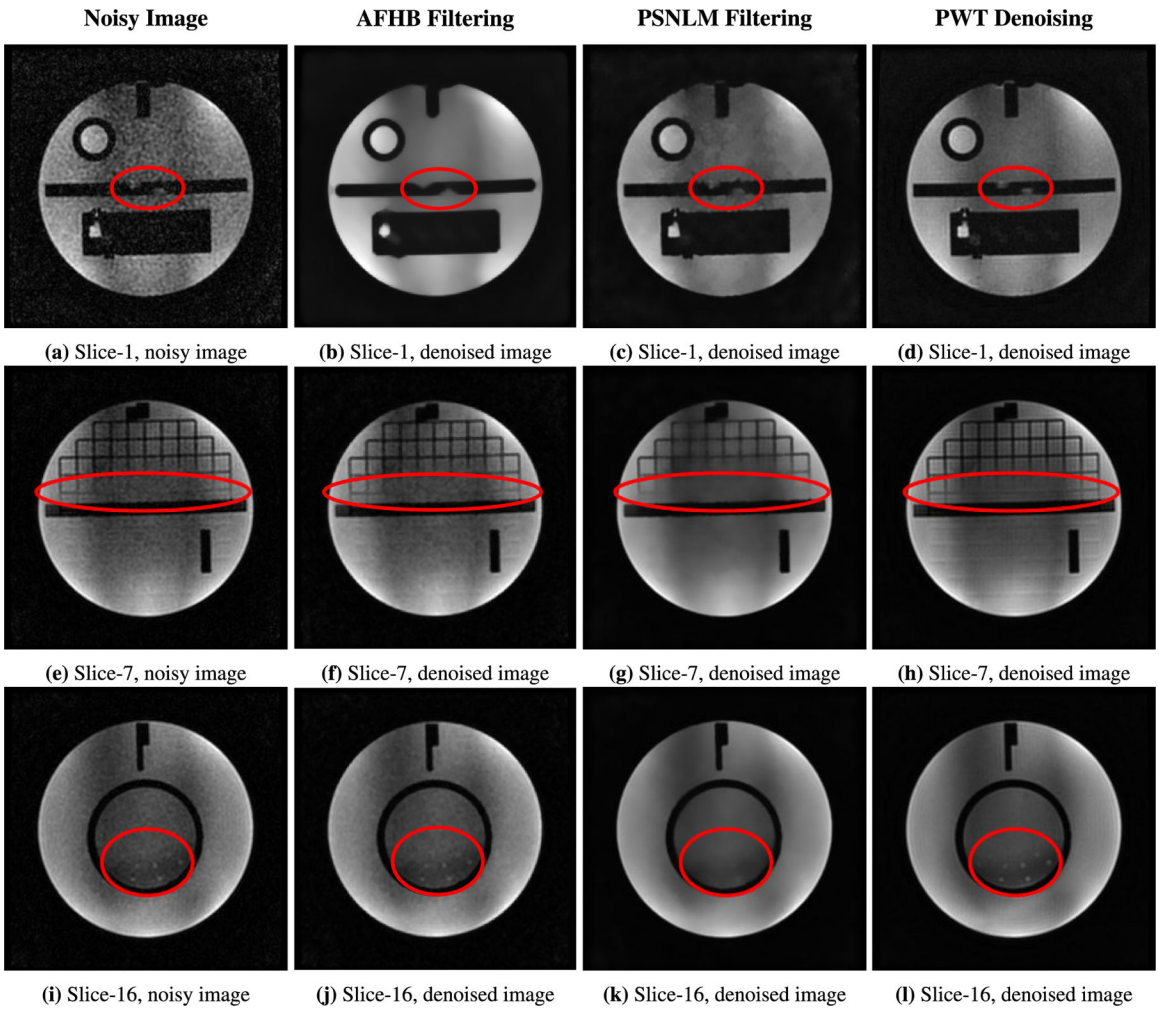

FIGURE 7.

Comparison of PWT with the adaptive fuzzy hexagonal bilateral and PSNLM filtering of slices 1 (first row), 7 (second row), and 16 (third row). Adaptive fuzzy hexagonal bilateral filtering is able to reduce noise but fails to recover features highlighted in the red ellipse. PSNLM filtering is able to recover features but they are difficult to identify without knowing they existed before. PWT is able to reduce noise as well as recover features. AFHB: Adaptive fuzzy hexagonal bilateral, PSNLM: Pre-smooth non-local means.

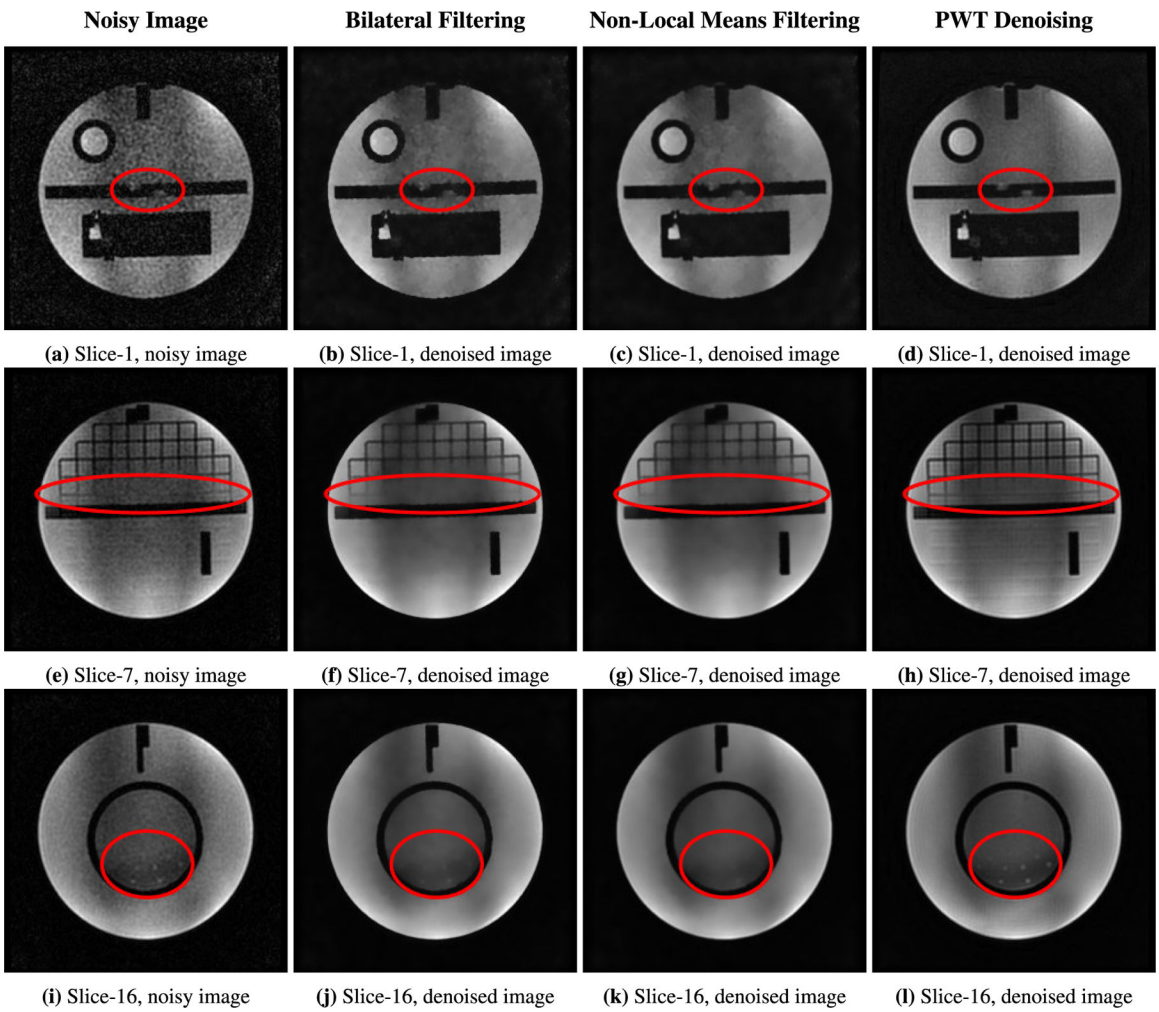

FIGURE 8.

Comparison of PWT with the bilateral and NLM filtering of slices 1 (first row), 7 (second row), and 16 (third row). Bilateral filtering is able to reduce noise but fails to recover features highlighted in the red ellipse. NLM filtering is able to recover features but they are difficult to identify without knowing they existed before. PWT is able to reduce noise and recover features.

TABLE 1.

Description of symbols used.

Symbol	Description
X	Input rectangular matrix.
X'	Denoised rectangular matrix.
U	Left singular vector matrix.
Σ	Singular value matrix.
V	Right singular vector matrix.
δ	Individual singular value.
λ	Threshold value.
$PSNR$	Peak Signal-to-Noise ratio.
P	Maximum possible value of image.
MSE	Mean Square Error.
R	Reference rectangular Matrix.
μ	Average.
σ	Standard Deviation.
S	Saturation Parameter.
n	Noise.
$\bar{n}$	Mean of noise.
RMS	Root Mean square value.
STD	Standard Deviation.

TABLE 2.

Mean of RMS and STD of noise. The mean RMS and mean STD are computed by taking the mean of RMS and STD of the 16 individual scans.

Slice	Mean RMS	Mean STD
1	26.67	16.56
2	26.45	16.56
3	27.72	17.18
4	26.36	17.28
5	27.56	17.45
6	27.73	17.77
7	28.57	18.09
8	30.36	18.43
9	29.57	18.41
10	28.81	18.48
11	29.40	18.53
12	29.31	18.52
13	28.63	18.29
14	29.25	18.11
15	28.91	17.88
16	27.84	17.70
17	27.43	17.18
18	26.41	16.58

TABLE 3.

Quantitative denoising results of the presented pixel-wise denoising method for phantom images of all slices.

	PSNR		SSIM		CNR	
Slice	**Noisy**	**Denoised**	**Noisy**	**Denoised**	**Noisy**	**Denoised**
1	65.30	80.17	0.37	0.94	7.78	37.24
2	65.36	80.00	0.41	0.95	9.62	47.47
3	64.91	78.93	0.42	0.95	12.16	58.53
4	64.75	78.32	0.45	0.96	14.18	64.69
5	64.81	78.35	0.46	0.96	16.50	74.91
6	64.47	78.05	0.47	0.96	17.01	80.32
7	64.20	76.78	0.54	0.97	17.25	71.92
8	64.01	77.31	0.62	0.98	17.72	78.85
9	64.09	77.80	0.45	0.96	20.44	98.39
10	63.98	78.08	0.45	0.96	20.48	105.25
11	63.81	77.82	0.44	0.96	20.60	103.79
12	63.86	77.78	0.44	0.96	20.06	104.59
13	64.00	77.58	0.48	0.96	20.58	97.83
14	64.17	77.09	0.48	0.96	22.12	92.18
15	64.35	77.37	0.48	0.96	20.70	94.09
16	64.55	77.36	0.49	0.96	19.75	89.37
17	64.78	78.25	0.48	0.97	20.47	86.76
18	65.15	78.17	0.49	0.97	21.91	95.28

TABLE 4.

Comparative quantitative results of Pixel-wise thresholding (PWT) with the AFHB and PSNLM filtering techniques. AFHB: Adaptive fuzzy hexagonal bilateral, PSNLM: Pre-smooth non-local means.

	PSNR				SSIM				CNR			
Slice	**Noisy**	**AFHB**	**PSNLM**	**PWT**	**Noisy**	**AFHB**	**PSNLM**	**PWT**	**Noisy**	**AFHB**	**PSNLM**	**PWT**
1	65.30	67.55	69.31	80.17	0.37	0.43	0.45	0.94	7.78	9.98	13.52	37.24
2	65.36	67.43	68.87	80.00	0.41	0.46	0.47	0.95	9.62	12.52	16.78	47.47
3	64.91	66.78	68.06	78.93	0.42	0.48	0.49	0.95	12.16	18.95	21.26	58.53
4	64.75	66.46	67.62	78.32	0.45	0.51	0.51	0.96	14.18	20.26	23.92	64.69
5	64.81	66.26	67.17	78.35	0.46	0.52	0.52	0.96	16.50	19.40	26.02	74.91
6	64.47	65.78	66.59	78.05	0.47	0.52	0.52	0.96	17.01	23.17	26.62	80.32
7	64.20	64.57	64.89	76.78	0.54	0.57	0.56	0.97	17.25	16.86	18.83	71.92
8	64.01	63.10	62.89	77.31	0.62	0.63	0.60	0.98	17.72	19.13	18.09	78.85
9	64.09	65.38	66.22	77.80	0.45	0.50	0.50	0.96	20.44	30.58	32.63	98.39
10	63.98	65.18	66.01	78.08	0.45	0.50	0.50	0.96	20.48	30.49	32.40	105.25
11	63.81	64.99	65.84	77.82	0.44	0.49	0.50	0.96	20.60	28.46	32.39	103.79
12	63.86	64.88	65.63	77.78	0.44	0.50	0.50	0.96	20.06	27.95	31.79	104.59
13	64.00	65.05	65.70	77.58	0.48	0.53	0.54	0.96	20.58	29.31	30.40	97.83
14	64.17	65.09	65.74	77.09	0.48	0.53	0.54	0.96	22.12	29.29	30.45	92.18
15	64.35	65.39	66.12	77.37	0.48	0.54	0.54	0.96	20.70	30.19	31.57	94.09
16	64.55	65.63	66.31	77.36	0.49	0.55	0.55	0.96	19.75	26.55	30.72	89.37
17	64.78	65.88	66.56	78.25	0.48	0.54	0.54	0.97	20.47	30.16	31.31	86.76
18	65.15	66.30	67.03	78.17	0.49	0.55	0.55	0.97	21.91	28.57	32.12	95.28

TABLE 5.

Efficacy comparison of the presented pixel-wise denoising method with AFHB and PSNLM. AFHB: Adaptive fuzzy hexagonal Bilateral, PSNLM: Pre-smooth non-local means.

	CPU Time (s)			Memory Usage (MBs)		
Slice	**AFHB**	**PSNLM**	**PWT**	**AFHB**	**PSNLM**	**PWT**
1	7.58	6.28	0.86	7.48	2382.73	128.25
2	7.81	6.73	1.00	7.48	2382.73	128.25
3	7.17	6.36	0.86	7.48	2382.73	128.25
4	6.96	6.66	0.98	7.48	2382.73	128.25
5	6.84	6.20	1.05	7.48	2382.73	128.25
6	6.52	6.69	0.83	7.48	2382.73	128.25
7	6.39	6.47	0.84	7.48	2382.73	128.25
8	6.75	6.55	0.86	7.48	2382.73	128.25
9	6.48	7.34	0.86	7.48	2382.73	128.25
10	6.55	8.20	0.78	7.48	2382.73	128.25
11	6.98	7.56	0.91	7.48	2382.73	128.25
12	6.59	10.30	0.92	7.48	2382.73	128.25
13	6.86	7.47	1.00	7.48	2382.73	128.25
14	6.72	7.53	0.81	7.48	2382.73	128.25
15	6.61	8.36	0.95	7.48	2382.73	128.25
16	6.67	7.44	0.89	7.48	2382.73	128.25
17	6.87	8.45	0.82	7.48	2382.73	128.25
18	6.66	8.41	1.02	7.48	2382.73	128.25

TABLE 6.

Root mean square and standard deviation of noise for noisy images of each slice and at all repetitions.

Repetition		1	2	3	4	5	6	7	8	9	10	11	12	13	14	15	16
Slice																	
1	RMS	29.24	27.22	30.55	25.94	27.41	24.86	23.22	25.70	30.16	25.32	27.26	23.71	26.48	25.03	28.02	26.67
	STD	17.71	17.55	17.66	15.97	16.18	16.10	16.08	17.36	17.72	16.04	15.98	16.07	15.95	16.19	16.18	16.14
2	RMS	26.91	26.00	25.14	30.27	25.41	27.48	27.44	26.36	27.04	29.78	27.73	23.04	25.44	25.26	23.55	26.42
	STD	17.59	17.35	17.82	16.11	16.34	16.02	16.27	17.23	17.35	16.24	16.13	16.06	16.19	15.98	16.16	16.19
3	RMS	31.99	31.11	28.05	29.24	26.12	23.90	27.73	29.00	26.21	29.54	27.63	27.73	26.18	28.28	23.99	26.85
	STD	18.51	17.81	18.17	16.55	16.80	16.65	17.98	17.98	17.85	16.52	16.69	16.62	16.78	16.48	16.80	16.74
4	RMS	27.04	28.80	26.30	29.07	25.44	24.54	26.39	26.82	26.79	28.57	23.99	26.15	24.10	24.32	25.79	27.70
	STD	18.85	18.03	18.16	16.63	17.13	16.73	17.99	17.80	18.08	16.53	16.47	16.79	16.82	16.71	16.79	16.92
5	RMS	29.41	29.95	32.02	26.94	28.74	25.03	26.03	27.22	28.12	29.14	25.23	26.88	27.60	25.06	25.41	28.21
	STD	18.75	18.45	18.35	16.88	16.95	16.68	17.92	18.03	18.12	16.75	17.03	16.82	17.13	17.10	17.24	17.07
6	RMS	30.23	28.80	26.57	31.37	26.57	28.61	26.48	28.51	29.61	27.38	26.09	29.61	24.63	25.97	27.32	25.88
	STD	19.49	18.60	18.50	17.25	17.55	16.92	18.09	18.32	18.28	17.06	17.28	17.21	17.58	17.28	17.48	17.46
7	RMS	33.61	32.58	31.44	30.90	25.38	29.88	25.91	27.67	27.92	29.00	27.89	28.34	25.58	27.67	27.13	26.18
	STD	20.13	18.75	18.99	17.47	18.07	17.06	18.47	18.47	18.46	17.01	17.48	17.76	17.84	17.69	17.89	17.91
8	RMS	34.51	31.08	32.28	29.58	29.75	29.68	27.99	31.87	30.37	32.54	25.32	28.77	28.70	30.65	31.04	31.58
	STD	20.57	19.11	19.25	17.84	18.21	17.67	18.82	18.78	18.90	17.29	17.75	18.06	18.17	18.02	18.19	18.28
9	RMS	30.23	33.34	32.32	30.90	27.70	28.64	27.63	28.05	30.93	29.92	28.77	30.09	26.30	30.51	31.15	26.63
	STD	20.36	18.95	19.41	17.92	18.26	17.44	18.87	18.73	18.72	17.41	17.73	18.14	18.17	18.19	18.01	18.21
10	RMS	32.69	33.96	27.92	30.34	26.91	29.31	29.68	28.74	27.92	30.23	25.20	29.68	30.83	25.94	25.88	25.67
	STD	20.63	19.21	19.53	17.97	18.31	17.68	19.19	18.67	18.99	17.29	17.67	18.33	18.01	18.05	17.94	18.18
11	RMS	33.03	35.03	29.95	28.25	28.15	27.38	29.47	27.79	27.29	28.28	28.80	28.97	30.55	28.12	30.06	29.31
	STD	21.00	19.21	19.55	18.16	18.02	17.62	18.83	18.68	18.90	17.63	17.98	18.19	18.10	18.14	18.26	18.19
12	RMS	34.19	32.88	29.07	28.90	26.30	30.37	28.70	28.57	28.87	30.02	27.76	26.45	29.88	28.90	27.32	30.76
	STD	20.97	19.21	19.26	18.17	18.30	17.65	19.07	18.97	18.98	17.53	17.82	18.10	18.13	18.12	18.07	18.04
13	RMS	34.04	29.85	32.81	27.67	25.91	26.79	26.70	29.07	28.38	29.92	29.04	26.48	26.09	27.92	27.73	29.71
	STD	20.65	19.48	18.95	17.74	18.05	17.32	18.57	18.53	18.44	17.40	17.58	17.79	17.91	17.80	18.14	18.30

Repetition		1	2	3	4	5	6	7	8	9	10	11	12	13	14	15	16
Slice																	
14	RMS	33.65	30.27	30.13	27.99	29.88	29.61	28.77	28.02	28.80	29.95	28.44	29.85	28.90	28.87	28.64	26.27
	STD	20.26	19.20	18.90	17.42	18.01	17.15	18.37	18.40	18.28	17.20	17.51	17.72	17.67	17.94	17.72	18.05
15	RMS	29.95	33.92	32.54	28.38	29.95	25.88	27.54	31.04	29.00	26.36	29.41	24.15	28.21	28.34	30.69	27.16
	STD	19.85	18.95	18.90	17.42	17.44	17.30	18.09	18.24	17.02	17.25	16.92	17.77	17.47	17.90	17.61	17.88
16	RMS	31.77	28.47	27.26	28.84	28.15	26.97	26.12	27.95	25.82	26.39	29.41	26.91	30.13	26.54	27.38	27.32
	STD	19.40	18.37	18.53	17.54	17.47	17.03	17.88	17.80	17.12	17.27	17.03	17.47	17.52	17.62	17.41	17.77
17	RMS	30.79	31.77	26.63	26.03	24.29	27.54	28.94	25.29	25.88	28.57	25.76	24.60	28.08	26.24	29.44	29.00
	STD	18.89	17.66	18.15	16.92	16.90	16.88	17.07	17.15	16.51	16.85	16.65	17.25	16.82	17.05	16.79	17.29
18	RMS	26.63	28.87	24.89	28.67	24.57	27.63	27.22	28.47	28.05	22.88	26.57	28.15	27.48	23.20	24.91	24.38
	STD	18.10	16.98	16.83	16.42	16.47	16.04	16.67	16.70	16.03	16.16	16.29	16.41	16.33	16.41	16.59	16.81

TABLE 7.

Comparative quantitative results of the presented pixel-wise denoising method with the bilateral and NLM filtering techniques.

	PSNR				SSIM				CNR				CPU Time		
Slice	**Noisy**	**Bilateral**	**NLM**	**PWT**	**Noisy**	**Bilateral**	**NLM**	**PWT**	**Noisy**	**Bilateral**	**NLM**	**PWT**	**Bilateral**	**NLM**	**PWT**
1	65.30	69.91	71.11	80.17	0.37	0.46	0.43	0.94	7.78	17.07	17.30	37.24	7.58	6.56	0.86
2	65.36	69.14	70.44	80.00	0.41	0.47	0.43	0.95	9.62	20.50	20.75	47.47	7.81	6.87	1.00
3	64.91	68.09	69.53	78.93	0.42	0.50	0.46	0.95	12.16	20.94	25.43	58.53	7.17	6.67	0.86
4	64.75	66.99	69.56	78.32	0.45	0.52	0.47	0.96	14.18	21.74	26.65	64.69	6.96	6.55	0.98
5	64.81	66.25	69.78	78.35	0.46	0.52	0.48	0.96	16.50	22.04	28.25	74.91	6.84	7.06	1.05
6	64.47	65.56	69.29	78.05	0.47	0.52	0.48	0.96	17.01	17.55	28.43	80.32	6.52	6.77	0.83
7	64.20	63.11	68.33	76.78	0.54	0.49	0.44	0.97	17.25	16.37	18.98	71.92	6.39	6.40	0.84
8	64.01	60.84	68.86	77.31	0.62	0.51	0.46	0.98	17.72	27.42	18.39	78.85	6.75	6.38	0.86
9	64.09	65.41	69.88	77.80	0.45	0.50	0.46	0.96	20.44	27.53	34.43	98.39	6.48	6.95	0.86
10	63.98	65.23	70.58	78.08	0.45	0.49	0.46	0.96	20.48	27.79	35.17	105.25	6.55	6.15	0.78
11	63.81	65.04	69.62	77.82	0.44	0.50	0.45	0.96	20.60	27.84	34.86	103.79	6.98	6.48	0.91
12	63.86	64.97	69.31	77.78	0.44	0.50	0.46	0.96	20.06	27.64	34.06	104.59	6.59	6.47	0.92
13	64.00	64.58	69.09	77.58	0.48	0.52	0.47	0.96	20.58	25.26	31.77	97.83	6.86	7.38	1.00
14	64.17	64.65	69.17	77.09	0.48	0.52	0.48	0.96	22.12	25.25	31.69	92.18	6.72	7.72	0.81
15	64.35	64.78	69.43	77.37	0.48	0.53	0.49	0.96	20.70	25.22	32.27	94.09	6.61	7.36	0.95
16	64.55	64.82	68.38	77.36	0.49	0.53	0.49	0.96	19.75	23.99	30.23	89.37	6.67	7.16	0.89
17	64.78	65.22	69.95	78.25	0.48	0.54	0.49	0.97	20.47	24.86	31.83	86.76	6.87	7.31	0.82
18	65.15	65.59	70.34	78.17	0.49	0.54	0.49	0.97	21.91	25.18	32.40	95.28	6.66	7.36	1.02